JACC: BASIC TO TRANSLATIONAL SCIENCE VOL. 3, NO. 1, 2018

PRECLINICAL RESEARCH

Diffusion Tensor Cardiac Magnetic Resonance Reveals Exosomes From Cardiosphere-Derived Cells Preserve Myocardial Fiber Architecture After Myocardial Infarction

Christopher T. Nguyen, PhD,[a,b] James Dawkins, DVM,[c] Xiaoming Bi, PhD,[d] Eduardo Marbán, MD, PhD,[c] Debiao Li, PhD[a,e]

VISUAL ABSTRACT

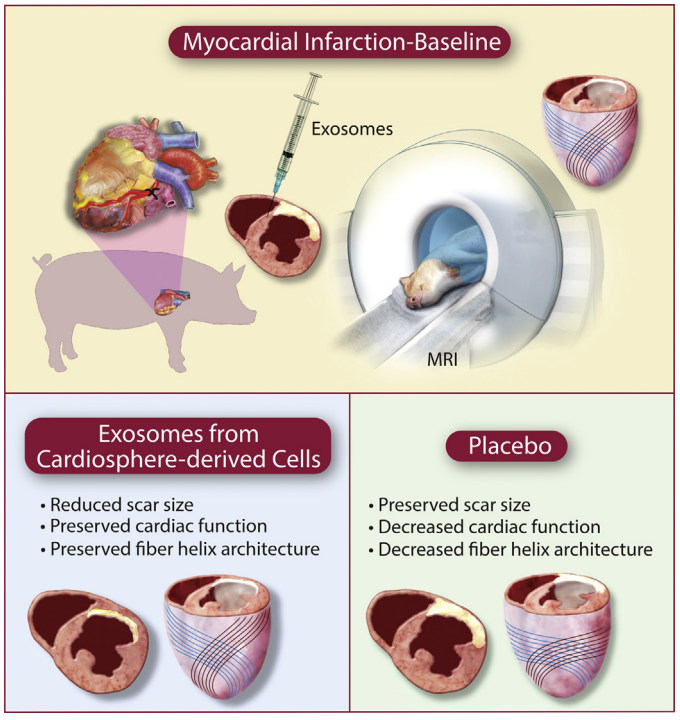

Nguyen, C.T. et al. J Am Coll Cardiol Basic Trans Science. 2018;3(1):97-109.

HIGHLIGHTS

- **CDC_{EXO} are RNA-laden nanoparticles that reduce scarring, halt adverse remodeling, and preserve cardiac function in rodents and pigs after MI.**
- **The therapeutic effects of CDC_{EXO} on myocardial fiber architecture and how it relates to preserved cardiac function and reduced scarring remain unclear.**
- **After intramyocardial CDC_{EXO} treatment in MI pigs, DT-CMR elucidated myocardial fiber architecture was preserved indicated by the unchanged helix angle transmurality.**
- **Scar size measured by conventional CMR combined with helix angle transmurality measured by DT-CMR demonstrated significant improvement in the prediction of cardiac function.**
- **DT-CMR is a powerful technology for myocardial regenerative therapy evaluation revealing unique insight into the myocardium's microstructure.**

From the [a]Biomedical Imaging Research Institute, Cedars-Sinai Medical Center, Los Angeles, California; [b]Cardiovascular Research Center, Cardiology Division, Massachusetts General Hospital, Harvard Medical School, Charlestown, Massachusetts; [c]Heart Institute, Cedars-Sinai Medical Center, Los Angeles, California; [d]MR R&D, Siemens Healthcare, Los Angeles, California; and the [e]Departments of Medicine and Bioengineering, University of California Los Angeles, Los Angeles, California. Dr. Bi is an employee of Siemens Healthcare. Dr. Marbán holds founder's equity in and serves as unpaid scientific advisor to Capricor Inc. All other authors have reported that they have no relationships relevant to the contents of this paper to disclose.

ISSN 2452-302X https://doi.org/10.1016/j.jacbts.2017.09.005

ABBREVIATIONS AND ACRONYMS

CDC = cardiosphere-derived cell

DT-CMR = diffusion tensor-cardiac magnetic resonance

EDV = end-diastolic volume

ESV = end-systolic volume

EF = ejection fraction

CDC_{EXO} = exosomes secreted by CDC

HA = helix angle

HAT = helix angle transmurality

|HAT| = absolute helix angle transmurality

ICC = intra-class correlation

LGE = late gadolinium enhancement

LV = left ventricular

MI = myocardial infarction

MRI = magnetic resonance imaging

ROC = receiver operating characteristic

ROI = region of interest

SS = scar size

TD = transmural depth

TE = echo time

TR = repetition time

SUMMARY

The object of the study was to reveal the fiber microstructural response with diffusion tensor cardiac magnetic resonance after intramyocardial exosomes secreted by cardiosphere-derived cells (CDC_{EXO}) in chronic porcine myocardial infarction. Porcine with myocardial infarction underwent intramyocardial delivery of human CDC_{EXO} and placebo in a randomized placebo-controlled study. Four weeks after injection, viability improved in the CDC_{EXO} group, whereas myocardial fiber architecture and cardiac function were preserved. In the placebo group, fiber architecture and cardiac function declined. Myocardial regeneration by CDC_{EXO} is not tumor-like; instead, details of tissue architecture are faithfully preserved, which may foster physiological excitation and contraction. (J Am Coll Cardiol Basic Trans Science 2018;3:97–109)

Cardiosphere-derived cells (CDCs) have demonstrated regenerative and cardioprotective properties in various animal models (1-6) of myocardial infarction (MI), and in patients as well (7,8). Specifically, CDCs decrease scar size (SS), increase viable tissue, and halt adverse remodeling. Underlying mediation of the regenerative benefits of CDCs has been associated with the secretion of exosomes (9-11).

SEE PAGE 110

These endogenous nano-scale lipid bilayer vesicles mediate cell-cell communication transferring microRNAs and other contents specific to the parent cell type (12). Exosomes secretion from CDCs (CDC_{EXO}) is necessary for the therapeutic benefits of CDCs, and CDC_{EXO} mimic the benefits of the parent CDCs (13-15). In a porcine model of convalescent MI, intramyocardial injections of CDC_{EXO} are beneficial by reducing SS, halting adverse ventricular remodeling, and preserving cardiac function (16), exhibiting a similar therapeutic benefit as intracoronary delivery of CDCs (17). However, the underlying mechanisms behind the regenerative properties of CDC_{EXO} remain to be revealed. One key feature of adverse ventricular remodeling during the healing phase following MI is the disruption of myocardial fiber architecture (18-20). It is currently unknown if CDC_{EXO} will affect myocardial fiber architecture post-MI. Preservation of correct fiber orientation following treatment with CDC_{EXO} could provide further insight into how cardiac function is maintained (or deteriorates) post-MI.

To characterize the impact of CDC_{EXO} on myocardial fiber architecture, a novel noninvasive technique is needed to monitor the therapy before and after delivery. One such technique is diffusion-tensor cardiac magnetic resonance (DT-CMR), which has demonstrated an ability to define myocardial microstructure before and after bone marrow-derived stem cell treatment in small animal MI models (21) and other potential cardiovascular therapies including left ventricular (LV) restoration (22), administration of *N*-acetylcysteine to treat cardiac hypertrophy (23), and human umbilical cord blood stem cell transplantation to treat MI (24). These preclinical studies demonstrated that a clear relationship exists between myocardial fiber architecture and cardiac function and that DT-CMR was sufficient to characterize such a relationship.

However, DT-CMR is not currently performed in a clinical setting because of major technical challenges centered on the inherent sensitivity of the technique to bulk motion. The previously mentioned DT-CMR-based therapy evaluation studies were in large part performed either in vitro or on small animal research magnetic resonance imaging (MRI) scanners capable of overcoming the deleterious effects of bulk motion. Recent technical advances have facilitated the acquisition in vivo of DT-CMR on clinical MRI scanners (25-29) in healthy human volunteers and large animals. Limited in vivo work has been performed preclinically in

All authors attest they are in compliance with human studies committees and animal welfare regulations of the authors' institutions and Food and Drug Administration guidelines, including patient consent where appropriate. For more information, visit the *JACC: Basic to Translational Science* author instructions page.

Manuscript received July 20, 2017; revised manuscript received September 11, 2017, accepted September 12, 2017.

large animal disease models (30,31) and in patients (32,33), which is even more technically challenging because of higher resting heart rates and subsequently more bulk motion.

A recent technical advance in compensating for second order bulk motion, which reduces the sensitivity of diffusion encoding to velocity and acceleration, demonstrated feasible DT-CMR imaging in healthy volunteers and patients with heart failure on a 3-T clinical scanner (34). This novel DT-CMR technique enables the investigation of the impact of CDC_{EXO} on myocardial fiber architecture in a preclinical setting with a large animal model. In this study, we apply the DT-CMR technique in a randomized placebo-controlled study of MI porcine treated with CDC_{EXO} on a clinical MRI system.

FIGURE 1 Study Design of the Randomized Placebo Controlled Study

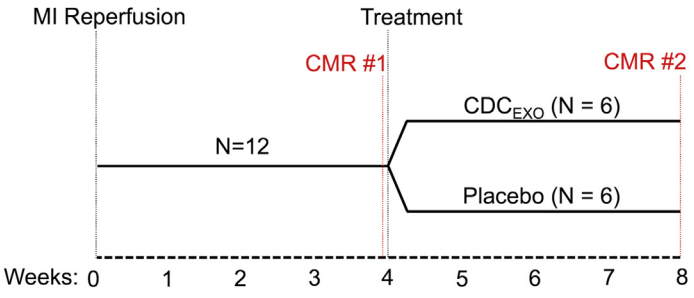

All subjects undergo MI reperfusion and after 4 weeks of recovery CMR is performed to establish baseline. After CMR scan 1, one-half the group is randomly chosen to be injected with CDC_{EXO} and the other one-half with a placebo. Both groups undergo a second CMR scan after 4 weeks post-injection. CDC_{EXO} = exosomes from cardiosphere-derived cells, CMR = cardiac magnetic resonance; MI = myocardial infarction.

METHODS

EXOSOME ISOLATION AND PREPARATION. Human CDC_{EXO} were isolated and prepared (7,10) from human heart specimens under a protocol approved by Cedars-Sinai Medical Center institutional review board for human subject research. Endomyocardial biopsies of the right ventricular aspect of interventricular septum were obtained from healthy hearts of deceased tissue donors. Biopsies were processed to isolate CDCs and exosomes were extracted from resulting CDCs. A detailed explanation can be found in the Supplemental Appendix.

RANDOMIZED PLACEBO-CONTROLLED STUDY DESIGN. MI was created in 12 female adult Yucatan mini-pigs under the approval of Cedars-Sinai Medical Center Institutional Animal Care and Use Committee. A balloon dilation catheter (TREK, Abbott Vascular, Santa Clara, California) was inserted into the left anterior descending coronary artery just below the first diagonal and inflated to achieve 100% occlusion of coronary blood flow for 150 min followed by reperfusion. During the occlusion, a continuous rate infusion of 2% lidocaine (2 mg/kg) was given. After 4 weeks post-reperfusion, CMR was performed to evaluate baseline microstructure, viability, and function before intramyocardial injection (**Figure 1**). Animals were randomized to receive intramyocardial injection of vehicle only (n = 6) or CDC_{EXO} (n = 6) in the border zone of the scar. Electroanatomic mapping of the left ventricle was performed using the NOGA cardiac navigation system (Biosense Webster, Inc., Diamond Bar, California) (16). The infarct border zone was identified using unipolar catheter tip potentials ranging between 4.1 and 7 mV. Animals were then followed for 4 weeks and imaged with CMR before sacrifice.

CMR IMAGING PROTOCOL. Animals were anesthetized and placed on a respiratory ventilator before imaging on a 3-T clinical MRI system (MAGNETOM Verio, Siemens Healthcare, Erlangen, Germany). CMR protocol included anatomical localizers (5 min), functional CMR (20 min), DT-CMR (25 min), and viability CMR (15-min delay and 20-min scan). Both functional and viability CMR covered the entire left ventricle with 10 to 12 short-axis slices.

Functional CMR (electrocardiogram-gated CINE balanced steady-state free precession: repetition time [TR]/echo time [TE] = 3.4/1.6 ms, $\alpha = 50^{\circ}$, 35 cardiac phases, 1.4 x 1.4 x 6 mm^3) was performed to yield LV volumes to calculate LV ejection fraction (EF). Performing functional CMR early in the protocol and adding long pauses (60 s) between each breath-hold ensured consistent heart rate across all slices.

DT-CMR (second-order motion compensated spin echo B1-resistant diffusion-prepared balanced steady-state free precession (34): TR_{group}/TR/TE = 2 RR/2.7 ms/1.5 ms, $\alpha = 90^{\circ}$, 1.6 x 1.6 x 10 mm^3, $Gradient_{max} = 43\sqrt{2}$ mT/m [2 gradients simultaneously slewed to max strength], b = 30 s/mm^2 + 6 x b = 350 s/mm^2) was acquired within a total 12 breath-holds covering the basal, mid, and apical short axis slices. Diffusion encoding was placed at the center of the end diastole identified by the functional CMR for all 3 slices. Interscan reproducibility (1 week apart) of the DT-CMR technique was measured in all subjects before MI was induced.

Viability CMR (late gadolinium enhancement [LGE] phase-sensitive inversion recovery fast low angle shot (35): TR/TE/inversion time [TI] = 326/1.47/300 ms, $\alpha = 20^{\circ}$, 1.3 x 1.3 x 6 mm^3) was performed 15 min

after a dose of gadolinium (0.2 mmol/kg, gadoversetamide, Optimark, Mallinckrodt Inc, St. Louis, Missouri) was injected following DT-CMR. After each breath-hold, the inversion time was increased by 5 ms to account for the increasing T1 of the contrast-enhanced scar tissue.

HISTOLOGY PROTOCOL. Following final CMR scan, the subjects were sacrificed in the operating room. Hearts were excised and placed in formalin for 3 days to ensure the heart was completely fixed. After fixation, the whole left ventricle was cut into 1-cm thick short axis slices with the mid short axis used for histological sectioning. A remote transmural section (1 cm in-plane width) opposite of the center of mass of the scar was isolated from the mid short axis slice (Supplemental Figure 1). The isolated remote section was further transmurally sectioned into 10-μm cuts from endocardium to epicardium. Five equidistant transmural cuts were chosen for conventional hematoxylin and eosin staining and commercial (PathScan Enabler IV, Meyer Instruments Inc., Houston, Texas) microscopy imaging (3.5 μm x 3.5 μm).

IMAGE ANALYSIS. Functional and viability CMR were processed using commercially available software (cvi42, Circle Cardiovascular Imaging Inc., Calgary, Canada) to semiautomatically segment the left ventricle. Functional CMR data were additionally manually segmented for all cardiac phases at end systole and end diastole to calculate the LVE) (36). The left ventricle and scar mass were manually segmented with a histologically validated (2) standardized method outlined by Society of Cardiovascular Magnetic Resonance (37) to calculate the normalized ($scar_{mass}/LV_{mass}$).

DT-CMR–derived myocardial fiber architecture was characterized by calculating the helix angle (HA) for each voxel using a custom software built on open source code (38). For normal myocardium, HA is typically positive in the endocardium and negative in the epicardium (20,39–41) (**Figure 2A**). For the chronic MI pig model, the remote myocardium overall exhibits a loss of positive HA in the endocardium with more severe loss closer to the infarct (18) (**Figure 2B**). The HA transmurality (HAT) or the slope of HA versus transmural depth (TD) was calculated only for remote myocardium as DT-CMR is not sufficient to resolve the complex collagen architecture in scar (42). The absolute value of HAT defined by absolute helix angle transmurality (|HAT|) was also characterized. A detailed explanation can be found in the Supplemental Appendix.

Further segmentation of the left ventricle was performed to identify the remote myocardium identified by viability CMR. Normalized changes (Δ = [pre-post]/pre) of calculated CMR parameters (ΔEF, ΔSS, and ΔHAT) pre- and post-therapy of the remote myocardial region were reported for the placebo and CDC_{EXO} treated groups. All segmentation was blinded to the treatment groups.

Structure tensor image analysis (43–45) was used on the histological transmural cuts to derive the fiber orientation at each transmural depth. Analogous to the DT-CMR data, HA and HAT were calculated for each subject using the primary eigenvector of the structure tensor. Comparisons with DT-CMR–derived HAT values were performed on a region of interest (ROI) spatially corresponding with the histological section (opposite of the center of mass of the scar in mid short axis slice). Five equidistant transmural HA values of this ROI were used to calculate HAT. Pearson correlation (R), intraclass correlation (ICC) (46), and Bland-Altman analysis (47) were performed to test the agreement between histology derived and DT-CMR–derived HAT values.

STATISTICAL ANALYSIS. Continuous variables were presented as mean ± SE. Wilcoxon signed-rank test was used to compare paired groups. Univariate linear regression was used to determine the relationship among ΔSS, ΔHAT, and ΔEF. Multivariate linear regression (Matlab, Mathworks, Natick, Massachusetts) was performed to determine the relationship between ΔEF and the combination of ΔSS and ΔHAT defined by: $\Delta EF = B_0 + B_1 \cdot \Delta SS + B_2 \cdot \Delta HAT$, where B_0, B_1, and B_2 are fitted coefficients. Receiver operator characteristic (ROC) analysis (Prism, GraphPad, La Jolla, California) was performed to determine the capability of ΔSS, ΔHAT, and ΔSS+ΔHAT to predict the therapeutic endpoint given by ΔEF. A positive/negative ΔEF indicates a beneficial/adverse therapeutic endpoint. All comparisons were 2-sided, and $p < 0.05$ was considered statistically significant. Median [interquartile range] were reported for all values.

RESULTS

IMAGE QUALITY AND REPRODUCIBILITY OF DT-CMR. The DT-CMR technique at the 0-, 4-, and 8-week time points qualitatively revealed no motion-induced signal loss in raw diffusion-weighted images (**Figure 2C**). Baseline HA maps before MI induction showed expected concentric transmural layers with right-handed helix fiber structure in the endocardium to left-handed helix fiber structure in the epicardium. The DT-CMR technique demonstrated substantial inter-scan reproducibility for |HAT| and LVEF (ICC = 0.74 and 0.71, respectively) (Supplemental Table 1).

FIGURE 2 **Cartoon Representations of the Myocardial Fiber Architecture**

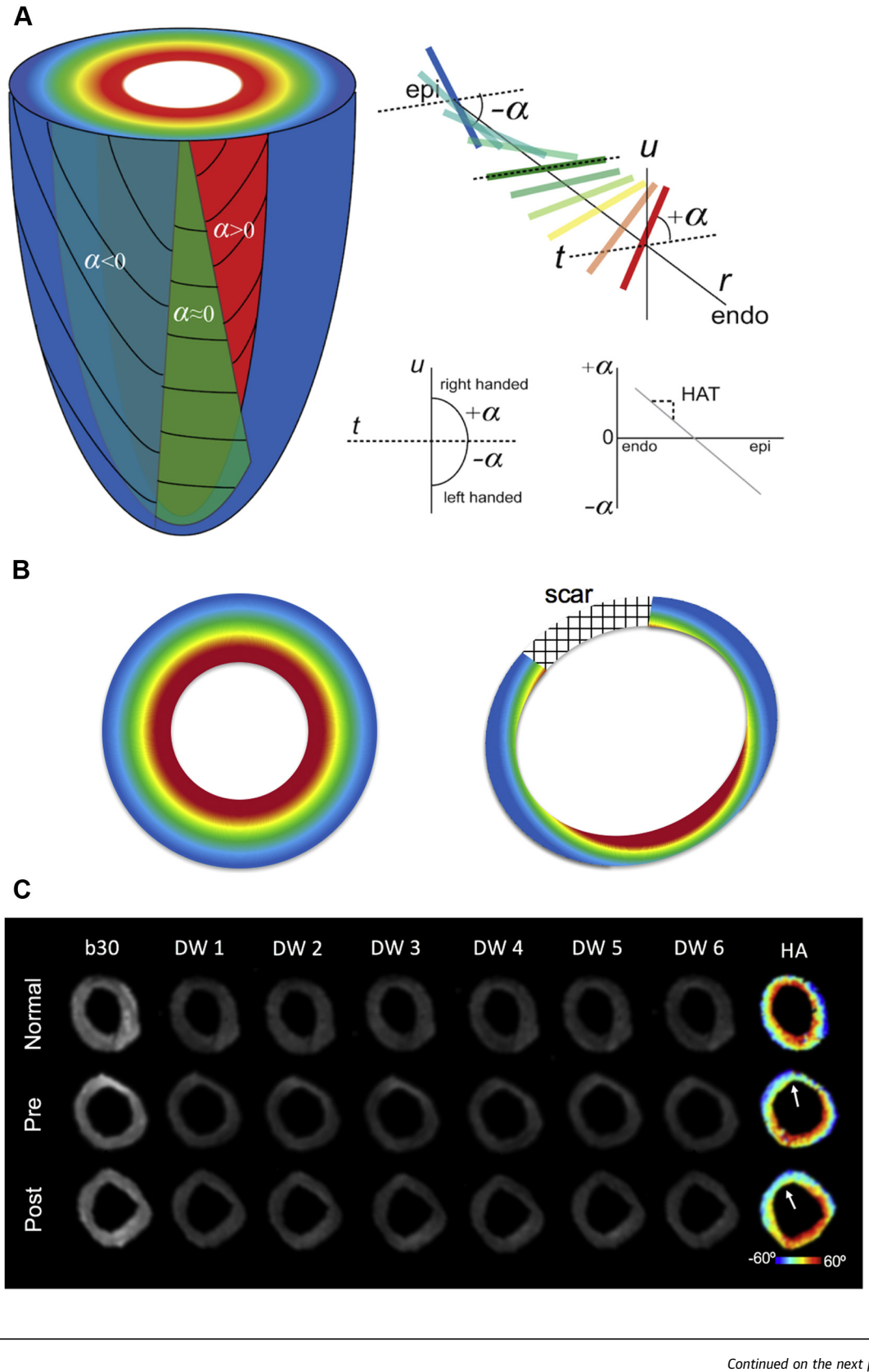

Continued on the next page

TABLE 1 Changes in Viability, Myocardial Fiber Architecture, and Cardiac Function

	CDC_{EXO}	Placebo
SS		
Pre (%)	17 (3)	19 (2)
Post (%)	13 (2)*	18 (3)
Δ (%)	−27 (9)†	−4 (13)
|HAT|		
Pre (°/%TD)	1.00 (0.06)	1.02 (0.07)
Post (°/%TD)	1.02 (0.06)*	0.91 (0.09)
Δ (%)	−2 (5)	−14 (4)†
LVEF		
Pre (%)	41 (3)	40 (6)
Post (%)	42 (5)*	35 (8)
Δ (%)	−2 (7)	−17 (6)†
LVEDV		
Pre (ml)	76 (12)	77 (16)
Post (ml)	84 (7)†	93 (18)
Δ (%)	16 (10)†	21 (10)†
LVESV		
Pre (ml)	45 (14)	46 (18)
Post (ml)	49 (4)*	63 (23)
Δ (%)	16 (14)†	32 (15)†
SV		
Pre (ml)	29 (2)	31 (2)
Post (ml)	34 (3)*	32 (6)
Δ (%)	9 (5)†	3 (5)

Values are median (interquartile range). *CDC_{EXO} vs placebo, $p < 0.05$. †pre vs post, $p < 0.05$. Significant ($p = 0.03$) reduction in scar size with preserved ejection fraction and helix angle transmurality were observed in the CDC_{EXO} group. Significant ($p = 0.03$ and $p = 0.03$, respectively) reduction in EF and helix angle transmurality with no change in scar size were observed in the placebo group.

Δ = normalized change (post − pre)/pre; CDC_{EXO} = exosomes of cardiosphere-derived cells; |HAT| = absolute helix angle transmurality; IQR = interquartile range; LVEDV = left ventricular end-diastolic volume; LVEF = left ventricular ejection fraction; LVESV = left ventricular end-systolic volume; post = post-treatment; pre = pre-treatment; SS = scar size; SV = stroke volume; TD = transmural depth.

CHANGES IN VIABILITY, MYOCARDIAL FIBER ARCHITECTURE, AND CARDIAC FUNCTION. At baseline, viability, myocardial fiber architecture, and cardiac function did not significantly differ between the CDC_{EXO} and placebo groups (CDC_{EXO}: SS = 17% [3%], |HAT| = 1.00°/%TD [0.06°/%TD], EF = 41% [3%]; placebo: SS = 19% [2%], |HAT| = 1.02°/%TD [0.07°/%TD], EF = 40% [6%]) (Table 1, Figure 3A). LV volumes at end-diastolic volume (EDV) and end-systolic volume (ESV) also did not significantly differ between the 2 groups at baseline (CDC_{EXO}: EDV = 76 [3] ml, ESV = 45 [14] ml; placebo: EDV = 77 [16] ml, ESV = 46 [18] ml).

In the CDC_{EXO} group after 4 weeks post-injection, viability significantly ($p = 0.03$) improved with a reduction in SS (13% [2%]) (Figures 3 and 4). Post-treatment myocardial fiber architecture (1.02°/%TD [0.06°/%TD]) and cardiac function (42% [5%]) did not significantly change from baseline. In 2 subjects, regional border zone HAT was seen qualitatively to be restored where SS was reduced (Figure 3, red arrows). However, quantitative regional analysis of HAT in the border zones across the entire CDC_{EXO} group still revealed no significant improvement.

In the placebo group after 4 weeks post-injection, viability did not change with a preserved SS (18% [3%]). Myocardial fiber architecture (0.91°/%TD [0.09°/%TD]) and cardiac function (35% [8%]) significantly ($p = 0.03$) declined. Plotting HA against transmural depth (Figure 5) demonstrated significant ($p = 0.02$) reductions in the absolute magnitude of HA in the inner 40% of the transmural layers. Reduction was also seen in the outer 20% of the transmural layer, but only trended toward significance ($p = 0.08$).

LV volumes significantly ($p < 0.05$) increased in both the CDC_{EXO} (ΔEDV = 16% [10%], ΔESV = 16% [14%]) and placebo groups (ΔEDV = 21% [10%], ΔEDV = 32% [15%]). Furthermore, the magnitude of the increase in LV volumes for the CDC_{EXO} group was significantly ($p < 0.05$) less than the increases in LV volumes for the placebo group.

Across all subjects, univariate linear regression between ΔHAT and ΔEF correlated moderately ($R^2 = 0.69$; $p < 0.01$) (Figure 6). ΔSS and ΔEF also correlated significantly ($p = 0.03$) but to a lesser degree in fit ($R^2 = 0.40$). ΔHAT had significant ($p = 0.03$) correlation ($R^2 = 0.39$) with ΔSS. Multivariate linear regression revealed that a substantial ($R^2 = 0.85$, adjusted $R^2 = 0.82$) correlation existed between ΔEF and the combination of ΔSS with ΔHAT ($B_0 = -0.055$ [−0.0104 to −0.0801], $B_1 = -0.25$ [−0.46 to −0.04], and $B_2 = 0.62$ [0.36 to 0.88]). Furthermore, ΔSS and ΔHAT

FIGURE 2 Continued

(A) Normal and **(B)** infarcted left ventricle. α characterizes the inclination of the estimated myocardial fiber orientation of each voxel in relation to the short axis plane (defined by *r* and *t*) and tangent plane (defined by *t* and *u*). For normal myocardial fiber architecture, the helix angle smoothly changes from the endocardium **(red)** to mid-myocardium **(green)** to epicardium **(blue)**. This transmural change is roughly linear and can be characterized by fitting a slope through α plotted against transmural depth yielding the HAT. For infarcted myocardium, the myocardial fiber architecture in the remote region exhibits less right-handed fibers in the endocardium ($\alpha > 0$) with a "flatter" overall HAT. **(C)** Representative image quality of the DW images from a single placebo subject before induced MI, baseline MI pre-injection, and post-injection. The DW images were used to reconstruct the diffusion tensor and subsequently used to derive HA. The **white arrow** points to the center of the scar. α = helix angle; DW = diffusion-weighted; HA = helix angle; HAT = helix angle transmurality.

FIGURE 3 Representative Images of LGE, CINE, HA Map, and |ΔHAT| p Value Wheel for Pre- and Post-CDC_{EXO} and Placebo Groups

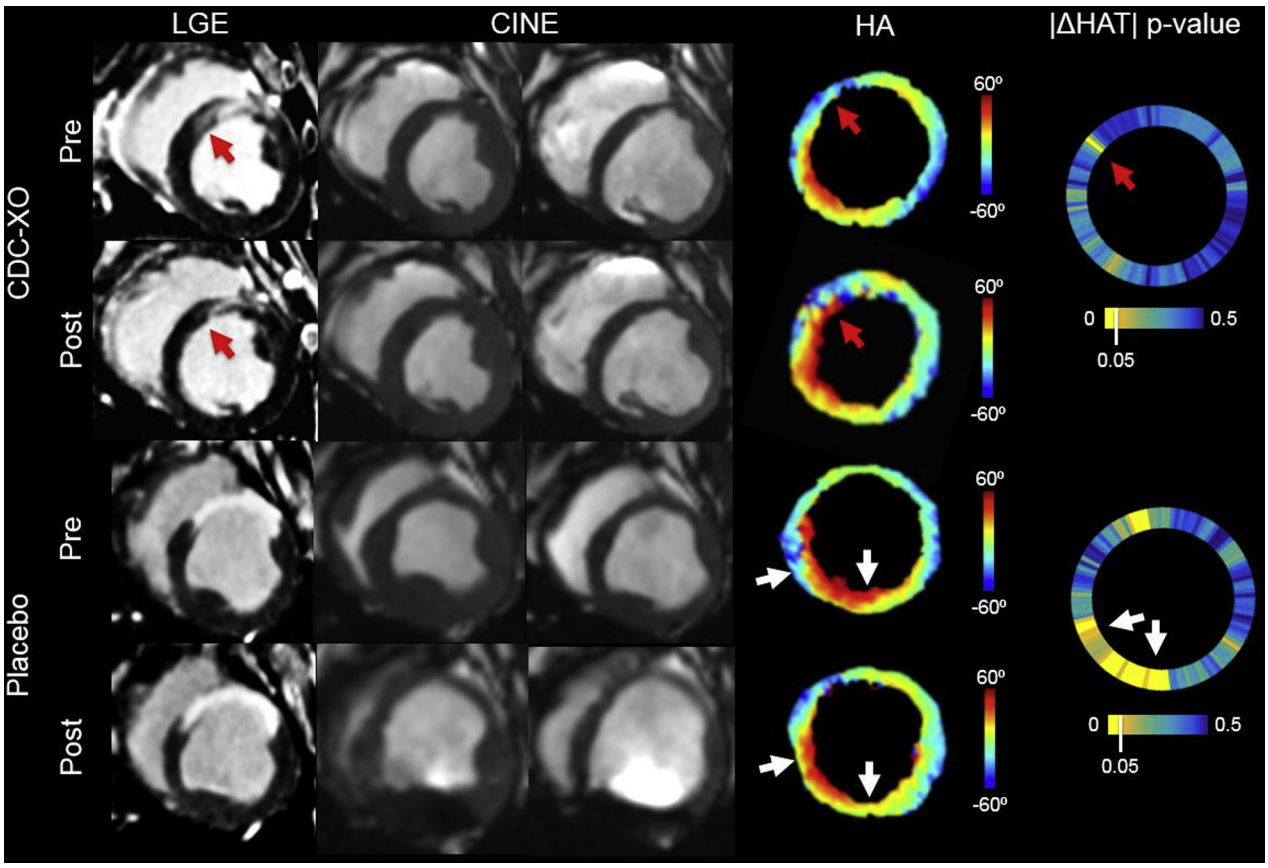

For the CDC_{EXO} subject, the red arrows point to a region of scar (anteroseptal) reduction in the LGE and a local restoration of the |HAT| with the endocardial fibers significantly ($p < 0.05$) changing from circumferential (HA ~ 0) to right-handed helical (HA > 0) orientation ($|HAT_{pre}| = 0.74°/\%TD$, $|HAT_{post}| = 0.95°/\%TD$). CINE revealed preserved LVEF. For the majority of the remote myocardium (anterolateral, inferolateral, inferior, and inferoseptal walls), |HAT| remained impaired with no significant change. For the placebo subject, LGE yielded no significant changes in scar size. CINE exhibited a reduction in LVEF. The |HAT| (white arrows) was significantly reduced in the inferoseptal wall with epicardial fibers changing from left-handed (HA < 0) to circumferential (HA ~ 0) orientation ($|HAT_{pre}| = 1.04°/\%TD$, $|HAT_{post}| = 0.78°/\%TD$). The |HAT| was also significantly reduced in the inferior wall with endocardial fibers changing from right-handed helical (HA > 0) to circumferential (HA ~0) orientation ($|HAT_{pre}| = 0.92°/\%TD$, $|HAT_{post}| = 0.69°/\%TD$). Anterolateral and inferolateral walls remained impaired with no significant change. CINE = cinematic magnetic resonance imaging; |HAT| = absolute helix angle transmurality; LGE = late gadolinium enhancement, TD = transmural depth; other abbreviation as in Figure 1.

were found to have modest interaction (B_1 and B_2) with a normalized covariance matrix value of −0.62.

HISTOLOGICAL VALIDATION OF DT-CMR. Both histological and DT-CMR results revealed the |HAT| of the placebo group (0.88°/%TD [0.2°/%TD] and 0.82°/%TD [0.1°/%TD], respectively) were significantly ($p = 0.02$, $p = 0.03$) less than the CDC_{EXO} group (1.08°/%TD [0.2]°/%TD and 1.08°/%TD [0.1°/%TD], respectively) (Figure 7). Furthermore, |HAT| derived from histology and DT-CMR were significantly ($p < 0.01$) correlated ($R^2 = 0.68$, ICC = 0.48). The Bland-Altman plot also demonstrated a high level of agreement with a slight negative bias (−0.03°/%TD).

PREDICTION OF THERAPEUTIC ENDPOINT. ROC analysis across all subjects revealed that ΔHAT and ΔSS had similar moderate predictive values of ΔEF (AUC = 0.66 [0.56 to 0.75] and 0.68 [0.52 to 0.73], respectively) (Figure 8). Comparing the individual ROC curves for ΔHAT and ΔSS yielded no significant difference. Combining ΔHAT and ΔSS using the fitted values of the multivariable regression ($B_0 = -0.055$, $B_1 = 0.25$, and $B_2 = 0.62$) led to an improved predictive value of ΔEF (AUC = 0.87 [0.73 to 1.065]) than either ΔHAT and ΔSS alone. A ROC plot of combined ΔHAT and ΔSS yielded significantly better sensitivity than either individual ROC for

FIGURE 4 Global Line Plots and Normalized Changes of SS, |HAT|, and EF for Both CDC_{EXO} and Placebo Groups

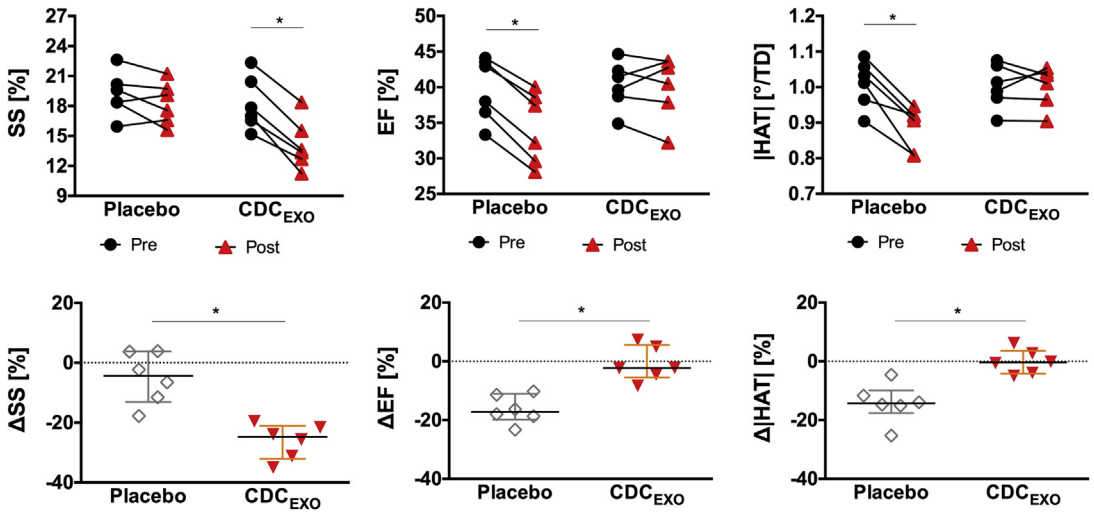

Global line plots **(top)** and normalized changes **(bottom)** demonstrate baseline values for SS, |HAT|, and EF were comparable between both groups. The CDC_{EXO} group exhibited significant ($p < 0.05$) reduction in SS but no significant changes in |HAT| and EF. The placebo group revealed significantly reduced |HAT| and EF but no change in SS. EF = ejection fraction; SS = scar size; other abbreviations as in Figures 1 and 3.

DHAT ($p = 0.01$) or ΔSS ($p = 0.03$) for all levels of specificity.

DISCUSSION

A randomized placebo-controlled study was carried out to characterize the impact of CDC_{EXO} therapy on myocardial fiber architecture and, more importantly, how possible changes in myocardial fiber architecture may correlate or predict changes in viability and cardiac function. This is the first study to investigate the microstructural impact of myocardial regenerative therapy in large animals using a clinical MRI system.

FIGURE 5 HA Versus TD Plots for Pre/Post Scans for the CDC_{EXO} and Placebo Groups

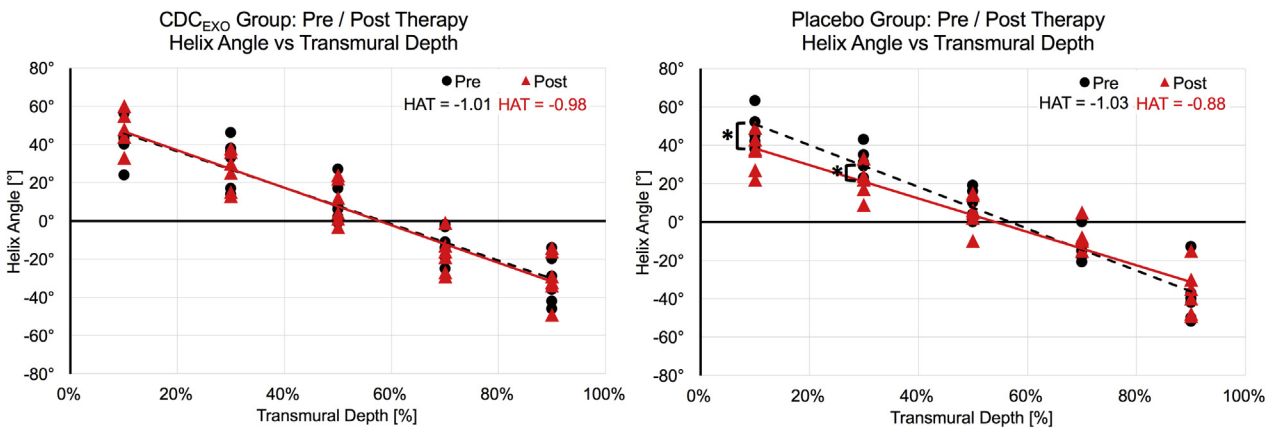

The calculated HAT (slope of the HA vs. TD line plot) did not significantly change in the treated group (−1.01°/%TD to −0.98°/%TD). In contrast, the placebo group exhibited a significant ($p = 0.03$) reduction in HAT (−1.03°/%TD to −0.88°/%TD) between the pre/post scans indicating an overall loss in helix transmurality. Furthermore, HA was significantly ($p = 0.03$ and $p = 0.04$, respectively) different at 10% and 30% TD between pre/post scans, with 90% TD trending toward significance ($p = 0.08$). Abbreviation as in Figures 1 and 3.

FIGURE 6 Univariate Linear Regression Plots

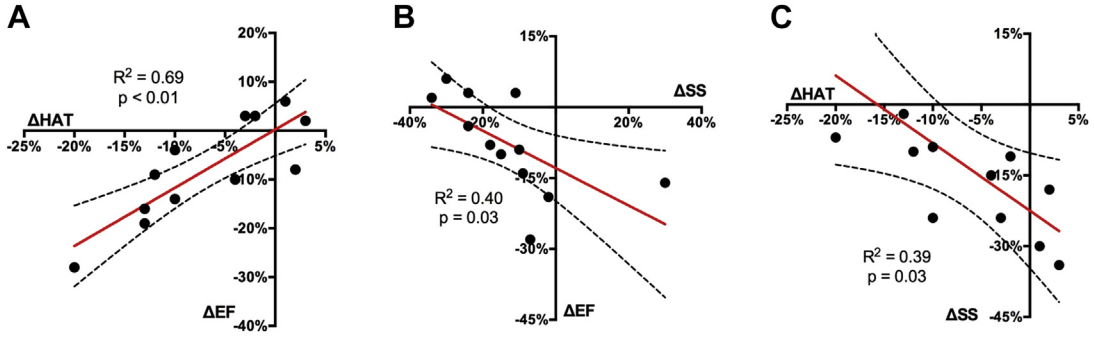

(A) ΔEF vs ΔHAT, **(B)** ΔEF vs ΔSS, and **(C)** ΔSS vs ΔHAT. ΔEF significantly ($p < 0.01$) and positively correlated ($R^2 = 0.69$) with ΔHAT, but significantly ($p = 0.03$) and negatively correlated ($R^2 = 0.40$) with ΔSS. ΔSS was significantly ($p = 0.03$) correlated ($R^2 = 0.39$) with ΔHAT. ΔEF = change in left ventricular ejection fraction; ΔHAT = change in helix angle transmurality; ΔSS = change in scar size.

FIGURE 7 Histological-Derived |HAT|

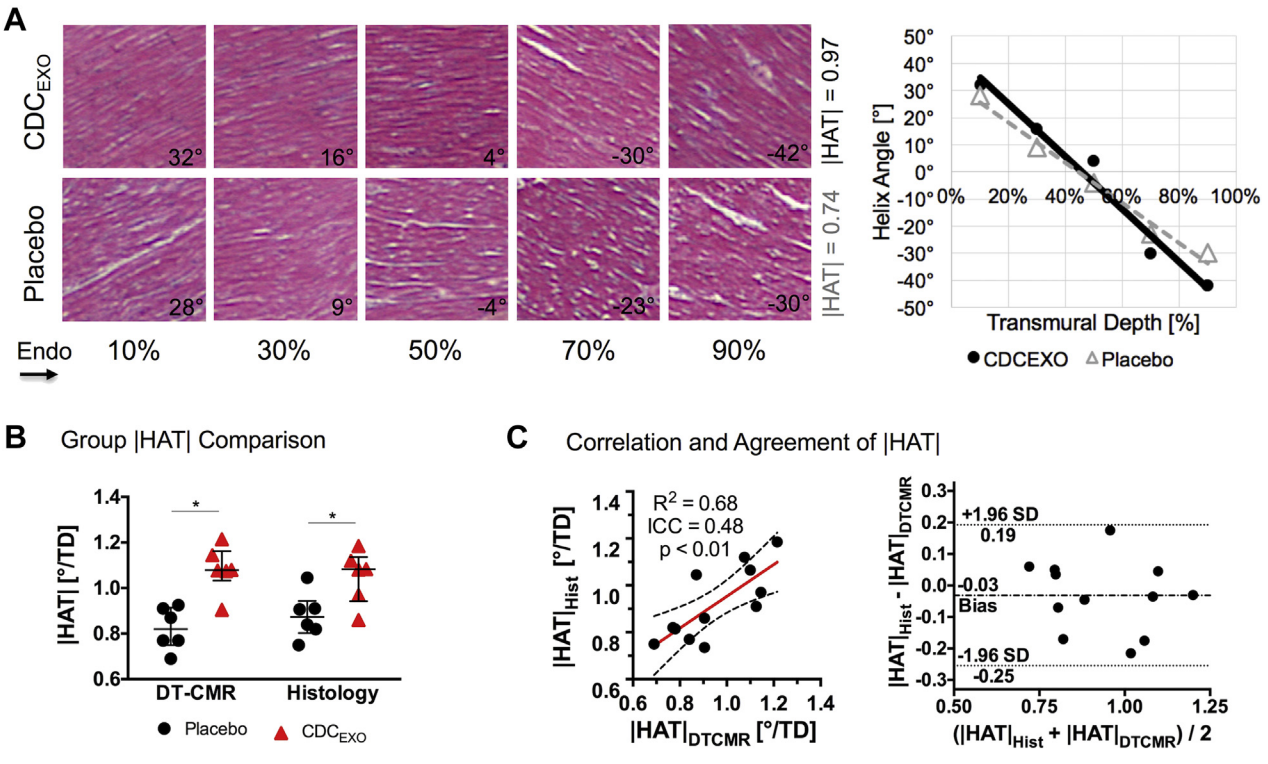

(A) Single representative case, **(B)** group comparison, and **(C)** correlation and agreement with DT-CMR–derived |HAT| values. The stained hematoxylin and eosin histological sections clearly show the orientation of the myocardial fibers at varying transmural depths, which can be quantified to yield a helix angle versus transmural depth plot and HAT values. Both DT-CMR and histology were concordant in exhibiting the same trend of a significant decreased |HAT| in the placebo group compared with the CDC_{EXO}-treated group. Furthermore, substantial correlation and agreement were found between histology and DT-CMR–derived |HAT| demonstrated in the correlation and Bland-Altman plot. DT-CMR = diffusion-tensor cardiac magnetic resonance. Abbreviation as in Figures 1 and 3.

FIGURE 8 ROC Curves of ΔSS, ΔHAT, and Combined ΔSS and ΔHAT to Predict ΔEF

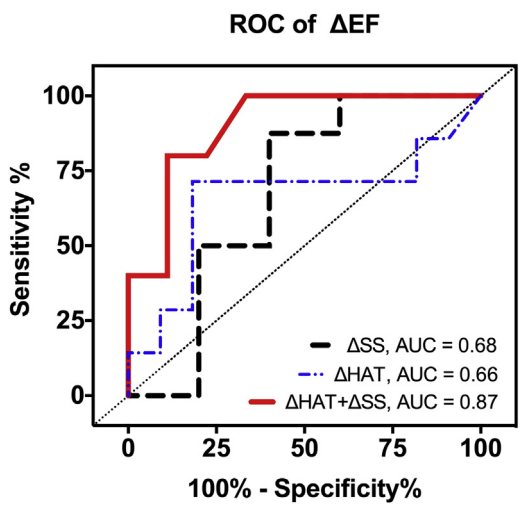

ΔHAT and ΔSS had comparable predictive values that did not significantly differ (AUC = 0.66 and 0.68, respectively). Combining ΔSS and ΔHAT with the best fit multilinear regression model resulted in significantly ($p = 0.04$) better predictive value (AUC = 0.87). AUC = area under the curve; ROC = receiver operator characteristic; other abbreviations as in Figure 6.

In the CDC_{EXO}-treated group, myocardial fiber architecture and cardiac function were preserved as evidenced by nonsignificant changes in HAT and EF from baseline, respectively. Viability significantly improved, with a reduction in SS. In the control group, myocardial fiber architecture and cardiac function adversely changed with significant reductions in HAT and EF, respectively. In contrast, viability did not significantly change exhibited by the preservation in SS. This is consistent with findings from other chronic MI porcine studies (18,20), in which SS stabilizes and both HAT and EF begin to deteriorate 4 weeks after induced MI. Furthermore, baseline HA maps for all subjects after 4 weeks of MI consistently exhibited loss of right-handed fibers in the endomyocardial layers in the remote tissue especially in the lateral wall, which was consistent with previous studies of porcine (18). The exact underlying mechanism of how both myocardial fiber architecture and cardiac function are preserved from CDC_{EXO} treatment remains to be revealed. One possible mechanism is that the location and orientation of the scar reduction may lead to muted remodeling of the myocardial fiber architecture and cardiac function. Location in this context does not refer to different coronary territories, but rather to the location within a single coronary territory. Studies on biomechanical modeling using finite element analysis supported by histology (48,49) have demonstrated that the location and orientation of the scar have a significant impact on the remodeling of cardiac function post-MI. Further longitudinal studies using a combined imaging approach will be needed to acquire the entire left ventricle with high-resolution 3-dimensional isotropic resolution DT-CMR and viability CMR monitoring the progression of scar orientation, scar location, and myocardial fiber architecture post-CDC_{EXO} treatment. Another mechanism is that CDC_{EXO} has demonstrated a significant decrease of percent collagen throughout the infarct, border zone, and remote areas of the myocardium (16), which have been associated with muted remodeling (50).

Changes in myocardial fiber architecture and viability did not significantly correlate across all subjects, but when combined yielded improved correlation and prediction to changes in cardiac function than either of the parameters alone. Furthermore, myocardial fiber architecture and viability exhibited nonsignificant interaction in the multivariate regression analysis. These findings suggest that myocardial fiber architecture of the remote tissue provided additional unique information to the measured viability in determining therapeutic efficacy defined by cardiac function. Moreover, characterizing the scar in conjunction with the myocardial fiber architecture of the remote tissue leads to a better prediction of overall global cardiac function. Further studies are warranted to understand how the additional information provided by myocardial fiber architecture characterization can be leveraged to potentially optimize the therapeutic efficacy of CDC_{EXO}.

Changes in myocardial fiber architecture and cardiac function were significantly correlated across all subjects, suggesting that myocardial fiber architecture and cardiac function are linked. Unfortunately, the design of the current study cannot provide insight into the potential causality of the observed relationship between cardiac fiber architecture and function, or if the 2 are affected by an additional unknown source. Future longitudinal studies with serial imaging are needed to further elucidate the directionality of a possible causal relationship or if a potential causal relationship between myocardial structure and cardiac function even exists at all.

STUDY LIMITATIONS. This study had several limitations related to the animal model, the DT-CMR technique, the DT-CMR-based HAT parameter, and the histological validation. Young healthy animals were used to create the chronic MI model. Although the chronic MI model itself exhibited the key features of MI with adverse remodeling and presence of scar, the

extrapolated effect of CDC_{EXO} in aged human patients with advanced cardiovascular disease is unclear. Furthermore, the chronic MI model combined with intramyocardial treatment required a substantial amount of resources, limiting the number of subjects and resulting in the study being relatively underpowered; therefore, the results of the study should be regarded provisional until they are reproduced in a larger study. Another limitation is the partial coverage of the left ventricle with the DT-CMR technique, which was circumscribed by the limited scan time for the study. Currently, in vivo application of DT-CMR is nascent; further technical refinement is ongoing to allow for DT-CMR to efficiently cover the entire left ventricle. However, the study revealed that even suboptimal LV coverage can still lead to sufficient characterization of global myocardial fiber architecture. Specific regional characterization will require a DT-CMR technique that is capable of full LV coverage and is warranted for future studies that are interested in studying the myocardial microstructure in the border zone of scar. The DT-CMR-based HAT parameter is limited with its sensitivity to the segmentation of epicardial and endocardial borders, which may increase variability when the DT-CMR images are noisy. Future studies should consider additional scan time in the form of more averages and/or DT-CMR directions to improve HA map image quality for more robust HAT quantification. The histological validation only sampled a single 1-cm transmural remote section in the mid short axis plane of the left ventricle directly opposite to the center of mass of the scar. This simplistic anatomic landmark was chosen due to the robust ability to identify the ROI on the DT-CMR images and could more easily spatially correspond with the histological sectioning in the presence of possible shrinkage of the tissue after fixation. Despite these limitations, significant correlation and agreement was found between DT-CMR and histology-derived HAT.

CONCLUSIONS

In a randomized, large animal study of chronic MI, exosomes from cardiosphere-derived cells demonstrated preservation of myocardial fiber architecture, reduction in SS, and attenuation of adverse remodeling associated with decreased cardiac function. Combining characterization of viability via scar quantification with myocardial fiber architecture of the remote tissue allowed for better correlation and prediction of the therapeutic end point of LV function than either of the two alone. Using in vivo DT-CMR to characterize myocardial fiber architecture provides unique additional information that is complementary to conventional viability characterization and can be performed on a clinical MRI system.

ADDRESS FOR CORRESPONDENCE: Dr. Debiao Li, Cedars-Sinai Medical Center, Biomedical Imaging Research Institute, 8700 Beverly Boulevard, Los Angeles, California 90048. E-mail: Debiao.Li@cshs.org.

PERSPECTIVES

COMPETENCY IN MEDICAL KNOWLEDGE: Heart disease remains the world's leading cause of death. Although great advances have been made over the past 25 years to improve patient survival, current treatment options to regenerate the myocardium are limited. Exosomes from CDC_{EXO} exhibit promising regenerative properties, but the effects on cardiac tissue are incompletely characterized. New imaging biomarkers such as myocardial fiber architecture mapping with DT-CMR MRI may further elucidate the therapeutic actions of CDC_{EXO}.

TRANSLATIONAL OUTLOOK 1: Recent uses of in vivo DT-CMR to characterize myocardial fiber architecture for therapy evaluation have been studied in small animals. Although large animals are used in this study, in vivo DT-CMR was implemented on a clinical MRI system and has already been tested in normal human volunteers and a small group of patients; therefore, the technique can readily be applied in patients.

TRANSLATIONAL OUTLOOK 2: Characterization of both myocardial fiber architecture and viability together may have added value in assessing the efficacy of therapy.

REFERENCES

1. Johnston PV, Sasano T, Mills K, et al. Engraftment, differentiation, and functional benefits of autologous cardiosphere-derived cells in porcine ischemic cardiomyopathy. Circulation 2009;120:1075–83.

2. Malliaras K, Smith RR, Kanazawa H, et al. Validation of contrast-enhanced magnetic resonance imaging to monitor regenerative efficacy after cell therapy in a porcine model of convalescent myocardial infarction. Circulation 2013;128:2764–75.

3. Gallet R, de Couto G, Simsolo E, et al. Cardiosphere-derived cells reverse heart failure with preserved ejection fraction in rats by decreasing fibrosis and inflammation. J Am Coll Cardiol Basic Trans Sci 2016;1:14–28.

4. Yee K, Malliaras K, Kanazawa H, et al. Allogeneic cardiospheres delivered via percutaneous transendocardial injection increase viable myocardium, decrease scar size, and attenuate cardiac dilatation in porcine ischemic cardiomyopathy editor. PLoS ONE 2014;9:e113805.

5. Cheng K, Malliaras K, Smith RR, et al. Human cardiosphere-derived cells from advanced heart failure patients exhibit augmented functional potency in myocardial repair. J Am Coll Cardiol HF 2014;2:49–61.

6. Smith RR, Barile L, Cho HC, et al. Regenerative potential of cardiosphere-derived cells expanded from percutaneous endomyocardial biopsy specimens. Circulation 2007;115:896–908.

7. Makkar RR, Smith RR, Cheng K, et al. Intracoronary cardiosphere-derived cells for heart regeneration after myocardial infarction (CADUCEUS): a prospective, randomised phase 1 trial. Lancet 2012;379:895–904.

8. Malliaras K, Makkar RR, Smith RR, et al. Intracoronary cardiosphere-derived cells after myocardial infarction: evidence of therapeutic regeneration in the final 1-year results of the CADUCEUS trial (CArdiosphere-Derived aUtologous stem CElls to reverse ventricULar dySfunction). J Am Coll Cardiol 2014;63:110–22.

9. Ibrahim A, Marbán E. Exosomes: fundamental biology and roles in cardiovascular physiology. Annu Rev Physiol 2016;78:67–83.

10. Ibrahim AG-E, Cheng K, Marbán E. Exosomes as critical agents of cardiac regeneration triggered by cell therapy. Stem Cell Rep 2014;2:606–19.

11. Vandergriff AC, de Andrade JBM, Tang J, et al. Intravenous cardiac stem cell-derived exosomes ameliorate cardiac dysfunction in doxorubicin induced dilated cardiomyopathy. Stem Cells Int 2015;2015:960926.

12. Théry C, Zitvogel L, Amigorena S. Exosomes: composition, biogenesis and function. Nat Rev Immunol 2002;2:569–79.

13. Sahoo S, Losordo DW. Exosomes and cardiac repair after myocardial infarction. Circ Res 2014;114:333–44.

14. Sahoo S, Klychko E, Thorne T, et al. Exosomes from human CD34(+) stem cells mediate their proangiogenic paracrine activity. Circ Res 2011;109:724–8.

15. Tseliou E, Fouad J, Reich H, et al. Fibroblasts rendered antifibrotic, antiapoptotic, and angiogenic by priming with cardiosphere-derived extracellular membrane vesicles. J Am Coll Cardiol 2015;66:599–611.

16. Gallet R, Dawkins J, Valle J, et al. Exosomes secreted by cardiosphere-derived cells reduce scarring, attenuate adverse remodelling, and improve function in acute and chronic porcine myocardial infarction. European Heart Journal 2016:ehw240.

17. Gallet R, Tseliou E, Dawkins J, et al. Intracoronary delivery of self-assembling heart-derived microtissues (cardiospheres) for prevention of adverse remodeling in a pig model of convalescent myocardial infarction. Circ Cardiovasc Interv 2015;8:e002391.

18. Wu EX, Wu Y, Nicholls JM, et al. MR diffusion tensor imaging study of postinfarct myocardium structural remodeling in a porcine model. Magn Reson Med 2007;58:687–95.

19. Wu M-T, Tseng W-YI, Su M-YM, et al. Diffusion tensor magnetic resonance imaging mapping the fiber architecture remodeling in human myocardium after infarction: correlation with viability and wall motion. Circulation 2006;114:1036–45.

20. Mekkaoui C, Huang S, Chen HH, et al. Fiber architecture in remodeled myocardium revealed with a quantitative diffusion CMR tractography framework and histological validation. J Cardiovas Magn Reson 2012;14:70.

21. Sosnovik DE, Mekkaoui C, Huang S, et al. Microstructural impact of ischemia and bone marrow-derived cell therapy revealed with diffusion tensor magnetic resonance imaging tractography of the heart in vivo. Circulation 2014;129:1731–41.

22. Walker JC, Guccione JM, Jiang Y, et al. Helical myofiber orientation after myocardial infarction and left ventricular surgical restoration in sheep. J Thorac Cardiovasc Surg 2005;129:382–90.

23. Lombardi R, Rodriguez G, Chen SN, et al. Resolution of established cardiac hypertrophy and fibrosis and prevention of systolic dysfunction in a transgenic rabbit model of human cardiomyopathy through thiol-sensitive mechanisms. Circulation 2009;119:1398–407.

24. Chen Y, Ye L, Zhong J, et al. The structural basis of functional improvement in response to human umbilical cord blood stem cell transplantation in hearts with postinfarct LV remodeling. Cell Transplant 2015;24:971–83.

25. Nielles-Vallespin S, Mekkaoui C, Gatehouse P, et al. In vivo diffusion tensor MRI of the human heart: reproducibility of breath-hold and navigator-based approaches. Magn Reson Med 2012;70:454–65.

26. Stoeck CT, Deuster von C, Genet M, Atkinson D, Kozerke S. Second-order motion-compensated spin echo diffusion tensor imaging of the human heart. Magn Reson Med 2016;75:1669–76.

27. Nguyen C, Fan Z, Sharif B, et al. In vivo three-dimensional high resolution cardiac diffusion-weighted MRI: a motion compensated diffusion-prepared balanced steady-state free precession approach. Magn Reson Med 2014;72:1257–67.

28. Aliotta E, Wu HH, Ennis DB. Convex optimized diffusion encoding (CODE) gradient waveforms for minimum echo time and bulk motion-compensated diffusion-weighted MRI. Magn Reson Med 2016;77:717–29.

29. Moulin K, Croisille P, Feiweier T, et al. In vivo free-breathing DTI and IVIM of the whole human heart using a real-time slice-followed SE-EPI navigator-based sequence: a reproducibility study in healthy volunteers. Magn Reson Med 2015;76:70–82.

30. Nguyen C, Fan Z, Xie Y, et al. In vivo contrast free chronic myocardial infarction characterization using diffusion-weighted cardiovascular magnetic resonance. J Cardiovasc Magn Reson 2014;16:1770.

31. Callot V, Bennett E, Decking UKM, Balaban RS, Wen H. In vivo study of microcirculation in canine myocardium using the IVIM method. Magn Reson. Med 2003;50:531–40.

32. Ferreira PF, Kilner PJ, McGill L-A, et al. In vivo cardiovascular magnetic resonance diffusion tensor imaging shows evidence of abnormal myocardial laminar orientations and mobility in hypertrophic cardiomyopathy. J Cardiovasc Magn Res 2014;16:445.

33. Nguyen C, Lu M, Fan Z, et al. Contrast-free detection of myocardial fibrosis in hypertrophic cardiomyopathy patients with diffusion-weighted cardiovascular magnetic resonance. J Cardiovasc Magn Res 2015;17:107.

34. Nguyen C, Fan Z, Xie Y, et al. In vivo diffusion-tensor MRI of the human heart on a 3 tesla clinical scanner: an optimized second order (M2) motion compensated diffusion-preparation approach. Magn Reson Med 2016;76:1345–53.

35. Kellman P, Arai AE, McVeigh ER, Aletras AH. Phase-sensitive inversion recovery for detecting myocardial infarction using gadolinium-delayed hyperenhancement. Magn Reson Med 2002;47:372–83.

36. Childs H, Ma L, Ma M, et al. Comparison of long and short axis quantification of left ventricular volume parameters by cardiovascular magnetic resonance, with ex-vivo validation. J Cardiovasc Magn Res 2011;13:40.

37. Schulz-Menger J, Bluemke DA, Bremerich J, et al. Standardized image interpretation and post processing in cardiovascular magnetic resonance: Society for Cardiovascular Magnetic Resonance (SCMR) board of trustees task force on standardized post processing. J Cardiovasc Magn Res 2013;15:35.

38. Garyfallidis E, Brett M, Amirbekian B, et al. Dipy–a novel software library for diffusion MR and tractography. Paper presented at: 17th Annual Meeting of the Organization for Human Brain Mapping 2011; January 26, 2011; Quebec City, Canada.

39. Sosnovik DE, Wang R, Dai G, Reese TG, Wedeen VJ. Diffusion MR tractography of the heart. J Cardiovasc Magn Res 2009;11:47.

40. Mekkaoui C, Reese TG, Jackowski MP, Bhat H, Sosnovik DE. Diffusion MRI in the heart. NMR Biomed 2015;30.

41. Mekkaoui C, Porayette P, Jackowski MP, et al. Diffusion MRI tractography of the developing human fetal heart. PLoS ONE 2013;8:e72795.

42. Sosnovik DE, Wang R, Dai G, et al. Diffusion spectrum MRI tractography reveals the presence of a complex network of residual myofibers in infarcted myocardium. Circ Cardiovasc Imaging 2009;2:206–12.

43. Budde MD, Frank JA. Examining brain microstructure using structure tensor analysis

of histological sections. NeuroImage 2012;63:1–10.

44. Budde MD, Annese J. Quantification of anisotropy and fiber orientation in human brain histological sections. Front Integr Neurosci 2013;7:3.

45. Khan AR, Cornea A, Leigland LA, Kohama SG, Jespersen SN, Kroenke CD. 3D structure tensor analysis of light microscopy data for validating diffusion MRI. NeuroImage 2015;111:192–203.

46. Rousson V, Gasser T, Seifert B. Assessing intra-rater, interrater and test-retest reliability of continuous measurements. Stat Med 2002;21:3431–46.

47. Bland JM, Altman DG. Agreement between methods of measurement with multiple observations per individual. J Biopharm Stat 2007;17:571–82.

48. Rouillard AD, Holmes JW. Mechanical regulation of fibroblast migration and collagen remodelling in healing myocardial infarcts. J Physiol 2012;590:4585–602.

49. Fomovsky GM, Rouillard AD, Holmes JW. Regional mechanics determine collagen fiber structure in healing myocardial infarcts. J Molec Cell Cardiol 2012;52:1083–90.

50. Cohn JN, Ferrari R, Sharpe N. Cardiac remodeling–concepts and clinical implications: a consensus paper from an international forum on cardiac remodeling. Behalf of an International Forum on Cardiac Remodeling. J Am Coll Cardiol 2000;35:569–82.

KEY WORDS diffusion tensor MRI, exosomes, fiber architecture, regeneration, myocardial infarction

APPENDIX For supplemental methods, figures, and a table, please see the online version of this paper.